ORIGINAL RESEARCH PAPER

The Institution of Engineering and Technology WILEY

Sparsity-based autoencoders for denoising cluttered radar signatures

Shobha Sundar Ram[1] | **Shelly Vishwakarma**[2] | **Akanksha Sneh**[1] | **Kainat Yasmeen**[1]

[1]Indraprastha Institute of Information Technology, New Delhi, India

[2]Department of Security and Crime Sciences, University College London, London, United Kingdom

Correspondence

Shobha Sundar Ram, Indraprastha Institute of Information Technology, New Delhi 110020, India.
Email: shobha@iiitd.ac.in

Funding information

Air Force Office of Scientific Research (AFOSR), Grant/Award Number: 5IOA036 FA23861610004

Abstract

Narrowband and broadband indoor radar images significantly deteriorate in the presence of target-dependent and target-independent static and dynamic clutter arising from walls. A stacked and sparse denoising autoencoder (StackedSDAE) is proposed for mitigating the wall clutter in indoor radar images. The algorithm relies on the availability of clean images and the corresponding noisy images during training and requires no additional information regarding the wall characteristics. The algorithm is evaluated on simulated Doppler-time spectrograms and high-range resolution profiles generated for diverse radar frequencies and wall characteristics in around-the-corner radar (ACR) scenarios. Additional experiments are performed on range-enhanced frontal images generated from measurements gathered from a wideband radio frequency imaging sensor. The results from the experiments show that the StackedSDAE successfully reconstructs images that closely resemble those that would be obtained in free space conditions. Furthermore, the incorporation of sparsity and depth in the hidden layer representations within the autoencoder makes the algorithm more robust to low signal-to-noise ratio (SNR) and label mismatch between clean and corrupt data during training than the conventional single-layer DAE. For example, the denoised ACR signatures show a structural similarity above 0.75 to clean free space images at SNR of −10 dB and label mismatch error of 50%.

1 | INTRODUCTION

Several types of urban radars have been researched and developed for civilian and military applications such as law enforcement, search and rescue, biomedical applications related to elderly monitoring and assisted living [1–6]. The primary objectives of most indoor radars are human detection and localization. Moving humans are detected based on the Doppler modulations that are introduced to coherent radar transmit waveforms. The movements of the limbs of the human introduce micro-Doppler features which are captured through single dimension Doppler-time spectrograms using joint time-frequency transforms [5, 7–10]. When the continuous wave radar is augmented with array processing, we obtain Doppler enhanced images along azimuth [11] or both azimuth and elevation [12, 13]. Alternatively, broadband pulse, linear frequency modulated or stepped frequency radars use fine downrange resolution to detect and track human motions along the range dimension [14–17]. The resulting radar signatures are either single dimension high range resolution

profiles (HRRP) (range-time signatures) [18] or range-enhanced higher order plots [19, 20]. Human activities are detected and interpreted on the basis of their micro-Doppler and micro-range features [3, 21–24].

Indoor radars could either be deployed in line-of-sight (LOS) environments (such as for fall monitoring of the elderly) or in non-line-of-sight (NLOS) environments (for security and surveillance purposes). The two most common NLOS deployments are the through-wall radar [1, 2, 25] and the around-the-corner radar (ACR) [26–30]. However, in both cases, the quality of radar signatures are greatly impacted by complex propagation artefacts introduced by walls such as the attenuation and multipath clutter [31–34]. We broadly categorize indoor clutter into two types-*target independent*, and *target dependent* static and dynamic clutter.

Target-independent static clutter arises from the reflections of the radar signal off the lateral walls, ground, ceiling and other furniture in the rooms. While the target dependent static clutter is generated through reflections and refraction of signals from the target to side and back walls, reverberations within

the front wall result in ghost targets and defocusing of targets. Several research efforts have been devoted to mitigate these artefacts on the radar signatures [35, 36]. The authors in [19, 20] used back-projection and sparsity-based change detection algorithms, respectively, to track slow-moving humans in the range-crossrange space in the presence of target-dependent static clutter. These techniques relied on the availability of prior information of the wall geometry and characteristics in indoor scenarios. Alternatively, authors in [37, 38] adopted the multipath exploitation strategy wherein the wall and target returns were projected on higher order subspaces based on their sparsity-based representations. Then, the wall effects were removed from the target returns. While this is an effective strategy for removing the target-independent static clutter, it cannot be used for the target-dependent clutter since the target and clutter returns are no longer independent of each other. Dynamic clutter, on the other hand, arises due to the presence of other movers in the channel (target independent dynamic clutter) or due to the interactions between the dynamic target and the channel (target-dependent dynamic clutter). The former can be separated on the basis of the micro-Doppler returns [39]. The latter is relatively difficult to remove as the target returns are not independent of complex wall propagation phenomenology.

Besides clutter, indoor radar signatures are also affected by noise and interference. Indoor radars typically operate below X band frequencies in order to enable radar signal penetration through the wall materials. These radars are federally mandated to transmit low powers to limit the possibility of electromagnetic interference with other wireless devices. On the other hand, these indoor radars may also encounter significant interference from neighbouring wireless systems in the environment such as WiFi. Therefore, successful radar detection of targets in these circumstances, rely on effective clutter, noise and interference management strategies. Here, we propose to use denoising autoencoders (DAEs) to recover high-quality radar signatures similar to free space signatures even under low signal to clutter and noise ratios (SCNRs).

DAE are neural networks with two stages—an encoder and a decoder as shown in Figure 1 [40]. During training, the encoder in the network is *trained* to represent a noisy image $(\widehat{x})$ with a hidden layer (Z). Then, the decoder is simultaneously *trained* to recover a clean/denoised image $(\widetilde{x})$ from the hidden layer that resembles a ground truth clean image (x). During the test, the encoder is fed with noisy images, and clean images are gathered at the output of the decoder. The DAE has been widely applied in many different fields such as computer vision [41, 42], anomaly detection and natural language processing [41, 43–45]. In [34], we demonstrated the usefulness of DAE for removing the dynamic clutter from through-wall frontal radar images. The algorithm demonstrated robust denoising and clutter mitigation performance for diverse wall and target conditions. However, the good performance of the network was predicated on two assumptions. First, the availability of a large volume of correctly labelled clean and noisy images during training. Second, the signal-to-noise ratio (SNR) of the radar system is high.

However, in real-world scenarios, both of these assumptions are often violated. For example, it may be nearly impossible to exactly replicate the same motion of the target in free space and then in the indoor channel conditions. Similarly, the channel may be plagued by high noise and interference, as discussed earlier. Therefore, we propose to use a stacked DAE with sparsity constraints on the hidden layer representations [40, 46], hitherto referred to as the StackedSDAE. In other words, instead of a single hidden layer, we propose a cascade of hidden layers, as shown in Figure 1b, where the representations are generated from sparsity-based constraints. The motivation of the approach is that such deeper representations enable the network to capture higher order abstractions in clean and noisy images. The incorporation of these additional hidden layers increases the computational time complexity during training but there is a significant reduction during *test* due to the feature size reduction within the hidden layers. Preliminary studies with the StackedSDAE were presented in [47]. Here, we offer a more comprehensive experimental evaluation of the proposed algorithm.

The proposed StackedSDAE can be used for *any* type of radar signature where corrupted and corresponding clean images are available. In this article, we have tested the proposed algorithm on different types of narrowband and broadband radar images of a dynamic human. First, ACR signatures are simulated using a combination of electromagnetic modelling using a full-wave solver and animation models of humans. Radar images are generated for different carrier frequencies and diverse electrical characteristics of the wall. The narrowband data are processed with short time Fourier transform across the time domain to obtain Doppler-time spectrograms. The wideband data are similarly processed with Fourier transform across the carrier frequency bandwidth to obtain HRRP. In the second scenario, we generate range enhanced frontal images of humans using wideband radar data augmented with two-dimensional array processing using an off-the-shelf sensor called the Walabot [48]. All of these images are corrupted by clutter and noise and the StackedSDAE is evaluated on them. Our results, across all three types of images, show that the StackedSDAE can considerably mitigate the clutter and distortions introduced by the walls even with a high labelling mismatch error and under low SNR.

To summarize, the main contributions are the following. First, we propose StackedSDAE for mitigating clutter and distortions introduced by different types of wall phenomenology. The framework of the proposed algorithm can be used to denoise any type of distorted radar signature. Second, we have performed experimental validation on three different types of radar signatures—the Doppler time spectrogram, the HRRP and the range enhanced frontal images. For this purpose, we have generated a large database of these radar signatures in diverse channel conditions and radar frequencies. The complete database and algorithms are shared with the research community on the following URL https://rb.gy/mmhzf6. Third, we have shown that the proposed algorithm is particularly effective under low SNR
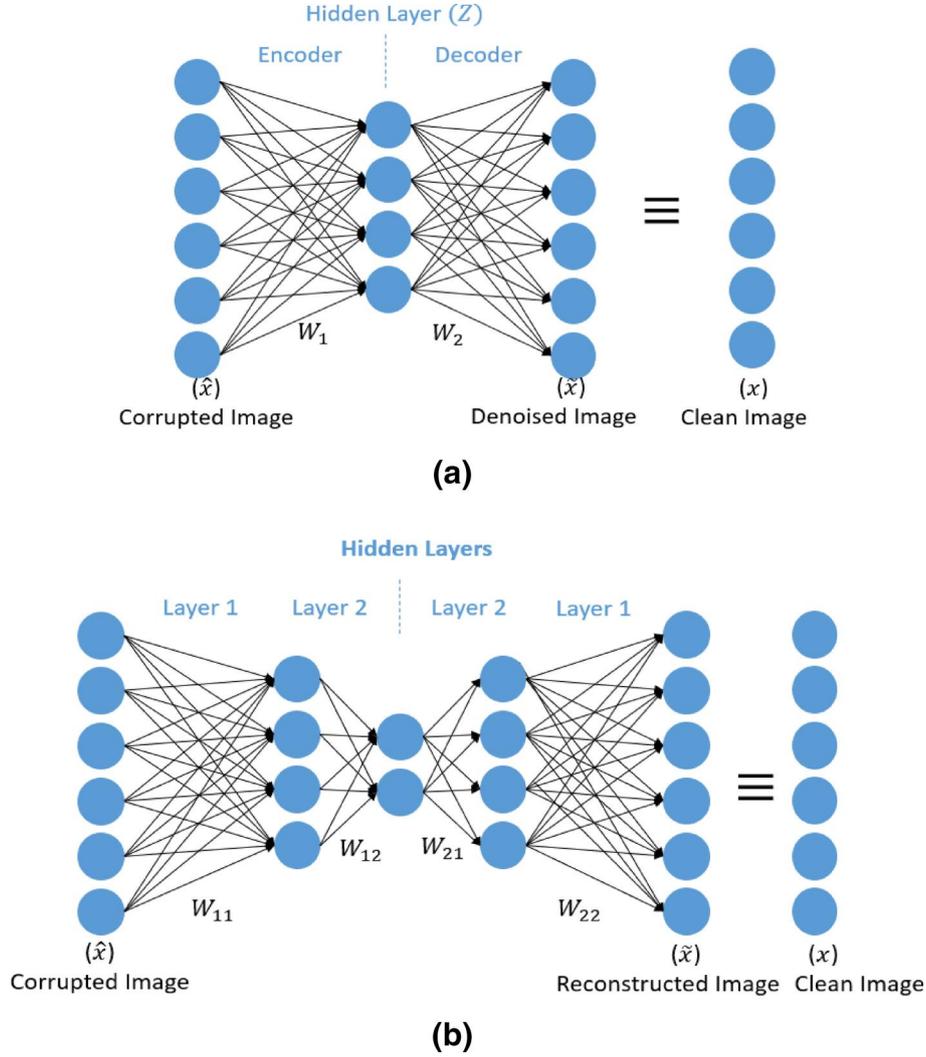
FIGURE 1 (a) Shallow denoising autoencoder and (b) Stacked denoising autoencoder

conditions and when there are large errors in the labelling of the training data.

The paper is organised in the following manner. In Section 2, we discuss the theory of StackedSDAE for clutter mitigation of radar images. In the subsequent section, we describe the experimental data generation through simulations followed by the simulation results in Section 4. In Section 5, we describe the measurement data collection followed by the denoising results from the autoencoder. We conclude with the analysis of the results in the final section.

Notation: Here, we represent scalars and column vectors by lower case letters and matrices by upper case letters.

2 | THEORY

When radars are operated in highly cluttered environments, significant distortions arise in the images. The DAE is a neural network that can be trained to remove the clutter artefacts from these images. The autoencoder requires both clean and noisy images while training. In the case of radar, the clean images correspond to radar images of the target in free space or some environment free of the clutter artefacts. These are denoted by $X \in \Re^{P \times Q}$ where P is the pixel size of each of the Q images. In other words, each image, x, of P pixels is vectorised and then Q such images are stacked column-wise to generate X. The corrupt data, $\widehat{X} \in \Re^{P \times Q}$ are corresponding images of a similar target undertaking a similar motion, gathered in cluttered environments. In this section, we describe the DAE and two variants, the sparsity-based DAE—termed as SparseDAE—and the sparsity-based stacked DAE—termed as StackedSDAE. Our hypothesis is that these variants will outperform the conventional DAE in clutter mitigation.

2.1 | Denoising autoencoder

We begin with a description of the conventional/standard single layer DAE framework, shown in Figure 1a. Here, the

algorithm learns a weight matrix, $W_1 \in \Re^{l \times Q}$, in order to represent $\widehat{X}^{tr}$ with a compressed $Z \in \Re^{l \times Q}$ through:

$$Z = \phi(W_1 \widehat{X}^{tr}). \tag{1}$$

The number of nodes, l, in the weight matrix is fewer than the original pixel size of the image. In the decoder, Z is mapped back to the reconstructed clean image, $\widetilde{X}^{tr}$ through:

$$\widetilde{X}^{tr} = W_2 \phi(W_1 \widehat{X}^{tr}), \tag{2}$$

where W_2 is the weighting function. In both the encoder and decoder, the same activation function ϕ, is used which could be either linear or a non-linear. Some of the popular non-linear activation functions in literature are hyperbolic tangent and sigmoid [49, 50]. The objective of the algorithm is to learn W_1 and W_2 from the training data such that the normalised mean square error between X^{tr} and $\widetilde{X}^{tr}$ is minimised as shown in:

$$\min_{W_1, W_2} \left\| X^{tr} - W_2 \phi(W_1 \widehat{X}^{tr}) \right\|_2^2. \tag{3}$$

Equation (3) is a complex optimization problem which is NP hard to solve. Therefore, we introduce a proxy variable, Z, as shown in:

$$\min_{W_1, W_2} \| X^{tr} - W_2 Z \|_2^2 \; s.t. \; Z = \phi(W_1 \widehat{X}^{tr}). \tag{4}$$

Then we relax the equality constraint in the formulation using an augmented Lagrangian, λ, in:

$$\min_{W_1, W_2, Z} \| X^{tr} - W_2 Z \|_2^2 + \lambda \left\| Z - \phi(W_1 \widehat{X}^{tr}) \right\|_2^2. \tag{5}$$

The regularisation parameter, λ, in the above expression trades off between the error in the encoder (second term) and the decoder (first term) stages. The above formulation has a close form solution using an alternating direction method of multipliers (ADMM) [51]. In the following section, we will describe the implementation of the ADMM in greater detail.

Once trained, the DAE is ready for test. During test, a denoised radar image $\widetilde{x}^{test}$ is recovered from the DAE with the test noisy image $\widehat{x}^{test}$ as input using Equation (2). The denoised image should now resemble the ground reference clean image x^{test}.

2.2 | Sparse denoising autoencoder (SparseDAE)

A modified autoencoder framework can be derived by imposing additional sparsity constraints on the hidden layer representations (Z) while learning the weighting matrices in the encoder and decoder. The objective function in Equation (5) is modified to:

$$\min_{W_1, W_2, Z} \| X^{tr} - W_2 Z \|_2^2 + \lambda \left\| Z - \phi(W_1 \widehat{X}^{tr}) \right\|_2^2 + \mu |Z|_1, \tag{6}$$

where an l_1 norm has been imposed on Z through a second regularisation parameter μ. The objective function is solved through ADMM by separately solving for W_1, W_2 and Z through iterations. First, W_1 is obtained from the closed form least squares solution for:

$$\min_{W_1} \left\| \phi^{-1} Z - W_1 \widehat{X}^{tr} \right\|_2^2. \tag{7}$$

Then W_2 is similarly solved using least squares in:

$$\min_{W_2} \| X^{tr} - W_2 Z \|_2^2. \tag{8}$$

Then both W_1 and W_2 are used to solve for Z in:

$$\begin{aligned} \min_Z \| X^{tr} - W_2 Z \|_2^2 &+ \lambda \left\| Z - \phi(W_1 \widehat{X}^{tr}) \right\|_2^2 + \mu |Z|_1 \\ &= \min_Z \left\| \begin{pmatrix} X^{tr} \\ \sqrt{\lambda} \phi(W_1 \widehat{X}^{tr}) \end{pmatrix} - \begin{pmatrix} W_2 \\ \sqrt{\lambda} I \end{pmatrix} Z \right\|_2^2 + \mu |Z|_1, \end{aligned} \tag{9}$$

using the iterative soft thresholding algorithm (ISTA) [52]. We update the network weight W_1, W_2 and proxy variable Z, iteratively until the algorithm converges.

Once the network is trained, the weight matrices W_1 and W_2 are used obtain a denoised form $\widetilde{x}^{test}$ of the corrupted test data $\widehat{x}^{test}$ using

$$\widetilde{x}^{test} = W_2 \phi(W_1 \widehat{x}^{test}). \tag{10}$$

The hypothesis is that when the autoencoder is properly trained the error after denoising (AD) between $\widetilde{x}^{test}$ and x^{test}, is lower than the error before denoising (BD) between $\widehat{x}^{test}$ and x^{test} where x^{test} is the corresponding ground truth clean image.

2.3 | Stacked sparse denoising autoencoder

In this framework, the single hidden layer representation within the autoencoder is converted to multiple stacked layers as shown in Figure 1b. There is a vast body of research that has demonstrated that additional deeper layers in a neural network enable capturing of higher order abstractions in the data resulting in significant improvement in the performance of the algorithms. This is because the successive layers result in the reuse of key features within the images as well as the extraction

of higher order features. The number of layers and the number of nodes within each layer are typically heuristically chosen. In our work, we implement the StackedSDAE using three hidden layers. Therefore, instead of learning just two weighting matrices as was the case of the shallow DAE, our objective here is to learn W_{11}, W_{12}, W_{21} and W_{22}. Each succeeding deeper layer is characterised by fewer number of nodes. As a result, the computational time complexity increases during the training phase since there are greater number of training matrices to learn. However, the complexity during the test phase reduces because of the reduced feature dimensions of the stacked layers.

Again, we divide our denoising problem into the training and the test stages. During training, the denoising problem can be formulated as

$$\min_{W_{11}, W_{12}, W_{21}, W_{22}} \left\| X^{tr} - W_{22}\phi\left(W_{21}\phi\left(W_{12}\phi\left(W_{11}\widehat{X}^{tr}\right)\right)\right) \right\|_2^2. \quad (11)$$

Again the problem is NP hard since it is non-convex. Similar to SparseDAE, we use the variable separation technique by introducing proxy variables Z_2, Z_1 and Z_0 such that

$$Z_2 = \phi(W_{21}Z_1) \quad (12)$$

$$Z_1 = \phi(W_{12}Z_0) \quad (13)$$

$$Z_0 = \phi(W_{11}\widehat{X}^{tr}) \quad (14)$$

Upon relaxing these constraints with augmented Lagrangian, the objective function now becomes

$$\min_{W_{11}, W_{12}, W_{21}, W_{22}, Z_2, Z_1, Z_0} \|X^{tr} - W_{22}Z_2\|_2^2$$
$$+ \mu_2\|\Phi^{-1}(Z_2) - W_{21}Z_1\|_2^2$$
$$+ \mu_1\|\Phi^{-1}(Z_1) - W_{12}Z_0\|_2^2$$
$$+ \mu_0\left\|\Phi^{-1}(Z_0) - W_{11}\widehat{X}^{tr}\right\|_2^2 \quad (15)$$

Again, we use the ADMM technique for solving the above formulation. We separately solve for W_{11}, W_{12}, W_{21} and W_{22}, using closed form expressions for least squares, as shown below

$$\min_{W_{11}}\left\|\phi^{-1}(Z_0) - W_{11}\widehat{X}^{tr}\right\|_2^2, \quad (16)$$

$$\min_{W_{12}}\left\|\phi^{-1}(Z_1) - W_{12}Z_0\right\|_2^2, \quad (17)$$

$$\min_{W_{21}}\left\|\phi^{-1}(Z_2) - W_{21}Z_1\right\|_2^2, \text{ and} \quad (18)$$

$$\min_{W_{22}}\left\|X^{tr} - W_{22}Z_2\right\|_2^2. \quad (19)$$

Then using the ISTA and the weighting matrices, we solve for Z_0, Z_1 and Z_2 based on the following objective functions:

$$\min_{Z_0}\left\|\phi^{-1}Z_1 - W_{12}Z_0\right\|_2^2 + \mu_0\left\|Z_0 - \phi(W_{11}\widehat{X}^{tr})\right\|_2^2$$
$$+ \lambda_0|Z|_1, \quad (20)$$

$$\min_{Z_1}\mu_2\left\|\phi^{-1}Z_2 - W_{21}Z_1\right\|_2^2 + \mu_1\|Z_1 - \phi(W_{12}Z_0)\|_2^2$$
$$+ \lambda_1|Z|_1, \text{ and} \quad (21)$$

$$\min_{Z_2}\|X^{tr} - W_{22}Z_2\|_2^2 + \mu_2\|Z_2 - \phi(W_{21}Z_1)\|_2^2 + \lambda_2|Z|_1. \quad (22)$$

Equations (16)–(22) are iterated till the algorithm converges.

Once the network weights are trained, we use them to reconstruct $\widetilde{x}^{test}$ from the corrupted $\widehat{x}^{test}$ by

$$\widetilde{x}^{test} = W_{22}\phi(W_{21}\phi(W_{12}\phi(W_{11}\widehat{x}^{test}))). \quad (23)$$

Note that the Stacked SDAE algorithm is significantly faster in generating denoised images at the test time as it involves only a simple product operation with reduced feature dimensions than DAE and Sparse DAE. This makes the algorithm suitable for real-time applications where training is usually done apriori.

2.4 | Evaluation metrics

The objective of the DAE and its variants are to reconstruct radar images that resemble those that would be obtained if the target were to move in free space conditions. Therefore, one obvious metric is the normalised mean square error between the reconstructed image ($\widetilde{x}^{test}$) which is obtained AD and the ground truth free space image (x^{test}). However, in the image processing community, other metrics are preferred to normalised mean square error (NMSE) since NMSE does not compare the salient features between different images. Here, we use the structural similarity index (SSIM) which is a popular metric that assesses luminance, contrast and structural differences between two images [53]. Its value ranges from 0 to one where one is obtained when the images are identical. We calculate SSIM between the cluttered image $\widehat{x}^{test}$ and x^{test} BD. Then the SSIM is calculated between $\widetilde{x}^{test}$ and x^{test} AD. The hypothesis, here, is that the SSIM will approach unity AD.

3 | SIMULATION METHODOLOGY

We test the denoising algorithms on indoor radar signatures obtained in NLOS scenarios where there is both noise and clutter. We specifically consider the ACR scenario for the simulations study as described below.
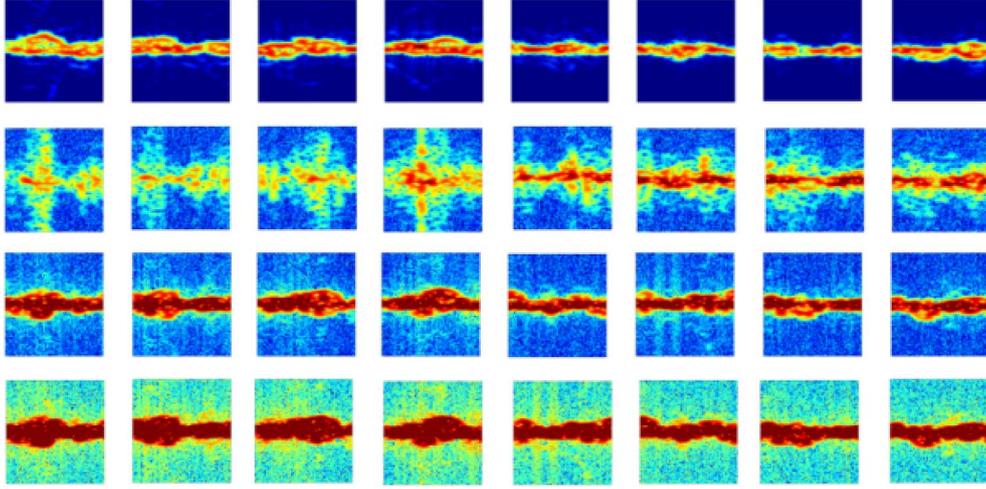
FIGURE 2 Simulation model of 6 s long human walking motion in around-the-corner radar (ACR) scenario in the presence of 20 cm thick walls with a dielectric constant of ϵ_r and conductivity of σ. Wave propagation from the radar source at (0.5,0) m modelled using two-dimensional full wave electromagnetic solver. LOS, line-of-sight; NLOS, non-line-of-sight

3.1 | Simulation models

The ACR simulation set up is shown in Figure 2. The electromagnetic wave propagation from the radar is modelled using two-dimensional finite difference time domain (FDTD) simulations in the XZ space enclosed by a perfectly matched layer (PML). The simulation space consists of two corridors of 2 m width arranged in a T-shape as shown in the figure. The walls are assumed to be 20 cm thick. The simulation space is discretised to form uniform grid cells that are a tenth of a wavelength (λ_c) of the carrier frequency (f_c). All the regions outside the walls are assumed to be free space. Stochasticity is introduced in the electrical characteristics of the walls. Each grid cell within the wall has a dielectric constant that is drawn from a normal distribution, $\mathcal{N}(\epsilon_r, \epsilon_r^{std})$, of mean ϵ_r and a standard deviation of ϵ_r^{std}. Similarly, the conductivity of each grid cell is drawn from the normal distribution of $\mathcal{N}(\sigma, \sigma^{std})$. Therefore, the walls are not truly homogeneous since each grid cell has slightly different electrical characteristics to model real-world conditions. The simulation space is bounded by a perfectly matched layer that is $2\lambda_c$ thick. The source excitation which models the monostatic radar is located at (0.5, 0) m. Two types of source excitation are considered. The first is a narrowband source modelled as a sinusoidal source of $f = f_c$ frequency. The second is a broadband source excitation ($f = f_c \pm \frac{\beta}{2}$) which is modelled as a Gaussian signal modulated by the sinusoidal carrier signal at f_c. The width of the Gaussian signal determines the bandwidth (β) of the source excitation. The time-domain simulations are allowed to run long enough to ensure that steady-state conditions are reached and the mean and standard deviation of the time-domain electric field at every point in the simulation space are saved [54]. Based on the normal distribution, multiple realisations ($\eta = 1: M$) of the time-domain electric field at each two-dimensional grid position, $\vec{\rho}$, are generated. Each of these η electric field vectors are then transformed using Fourier transform to the frequency domain and complex responses, $H(\vec{\rho}, f, \eta)$, at $f = f_c \pm \frac{\beta}{2}$, are saved.

Next, we consider the human moving along the tangential trajectory before the radar, as shown in the figure, over a duration of T seconds. The human is a three-dimensional figure with the height along Y axis. The skeleton framework of the human and the animation motion of the body parts are described using motion capture data from Sony [55]. Then the electromagnetic radar scattering off the human is modelled using the techniques described in [56]. We briefly describe the technique here. The human is considered to be a collection of B discrete point scatterers corresponding to different body parts each of a_b reflectivity. Each of the body parts is modelled as an ellipsoid whose radar cross-section (a_b^2) is obtained with analytical expressions. The time-domain radar returns from the human, corresponding to each η stochastic FDTD realisation at frequency f, are obtained by

$$s_{rx}(t, f, \eta) = \sum_{b=1}^{B} A a_b H(\vec{\rho}_b(t), f, \eta)^2 e^{-j4\pi \frac{f}{c}(r_b(t) - \rho_b(t))},$$
$$t = 0: T, f = f_c \pm \beta, \eta = 1: M. \quad (24)$$

Here, $r_b(t)$ and $\rho_b(t)$ are the time-varying three- and two-dimensional Euclidean distances of the bth point scatterer from the radar respectively. The two-way propagation physics from the radar to the point scatterer is captured by the square of the wall response H. Since, the FDTD is a two-dimensional simulation with an infinite line source excitation, the exponential phase term in Equation (24) corrects the circular phase front from the two-dimensional FDTD propagation physics to the spherical phase front in the three-dimensional scenario. A in the above expression calibrates the amplitude of the FDTD source excitation to desired radar equivalent isotropic radiated power.

The time-domain radar data, $s_{rx}(t, f, \eta)$, could be either narrowband or wideband. In the case of narrow-band data

FIGURE 3 Doppler-time spectrograms of human walking in ACR scenario with monostatic narrowband radar operating at **2.4 GHz**. The *y*-axis across all figures shows Doppler frequencies spanning from −250 to +250 Hz. The *x*-axis across each figure is of 0.75 s duration with a total time duration of 6 s across the eight columns. The dynamic range of each figure is from −20 to −70 dB. The first, second, third and fourth rows show the radar signature of human walking in the free space, low conductive, medium conductive and high conductive wall conditions, respectively. SNR for all figures along the bottom three rows is fixed at –20 dB. ACR, around-the-corner radar; SNR, signal-to-noise ratio

(where $\beta = 0$), the short-time Fourier transform is applied on the data to obtain M Doppler spectrograms, x_{DT}, as shown in

$$x_{DT}(\tau, f_D, \eta) = \int_t s_{rx}(t, \eta) w(\tau - t) e^{-j2\pi f_D t} dt, \eta = 1 : M, \quad (25)$$

where $w(t)$ is the short time window function. In the case of the broadband data, Fourier transform is applied across the bandwidth of the data at every time instant t to obtain M HRRP, x_{HRRP}, as shown in

$$x_{HRRP}(t, r, \eta) = \int_f s_{rx}(t, f, \eta) e^{+j2\pi f \frac{2r}{c}} df, \eta = 1 : M. \quad (26)$$

3.2 | Simulated radar signatures

3.2.1 | Narrowband Doppler-time Signatures

The above process is carried out independently for three radar carrier frequencies -f_c : 2.4 , 5 and 10 GHz - and the radar bandwidth is set at 0 Hz. For each of the above cases, we consider three different types of walls. A wall with low mean conductivity $\sigma = 0.05$ S/m, medium conductivity ($\sigma = 100$ S/m) and high conductivity ($\sigma = 1e5$ S/m). The mean dielectric constant is fixed at $\epsilon_r = 4$. The standard deviation for both the dielectric constant and conductivity are fixed at 30%. Twenty stochastic realisations of the time-domain electric field are generated for each of the three cases using the stochastic FDTD solver. These realisations are combined with the human walking motion to generate ACR Doppler-time signatures. A short time window of 0.1 s is used to generate the spectrograms. The total duration of human motion is 6 s. This interval is separated into eight consecutive intervals of 0.75 s duration. The sampling frequency of the time domain data is

500 Hz resulting in Doppler frequency axes spanning from $f_D = -250$ Hz : + 250 Hz in all the images. Then complex Gaussian additive noise, $\mathcal{N}(0, N_p)$, of N_p noise power is added to each pixel of the images to realize 200 images. Therefore, we have a total of 1600 images for each of the three wall cases.

We show the wall propagation effects on the images at 2.4 GHz in Figure 3. The top row on the figure shows the results generated in free space conditions in the absence of clutter and noise. These are generated when the human walks in the presence of radar but without any walls. The resulting micro-Doppler spectrograms across eight time intervals from 0 to 6 s are shown. We observe that the Dopplers are low since the human motion is tangential with respect to the radar. As the human approaches the radar, from 0 s to approximately 3 s, the Dopplers are positive. Then, when the human moves away, the Dopplers become negative. We observe weak micro-Doppler returns from the other body parts. The second row shows the returns when the human is walking in the presence of low conductive walls. In this scenario, the walls allow the signal to penetrate with some attenuation. Hence, the strength of the signals is weaker. Due to the multipath introduced by the ringing of the radar signal within the wall, we observe a lot of multipath. From this figure, it becomes difficult to know whether there are one or more targets moving and whether they are coming towards or away from the radar. The third and fourth row show the micro-Dopplers from a medium and a high conductive wall. Due to the lossy nature of the walls, the through-wall propagation is blocked. Instead, the dominant phenomenon here is the reflections off the lateral walls which give rise to high strengths in the radar scattered signal. There is a lesser micro-Doppler spread, in these cases. However, we do observe some negative Dopplers due
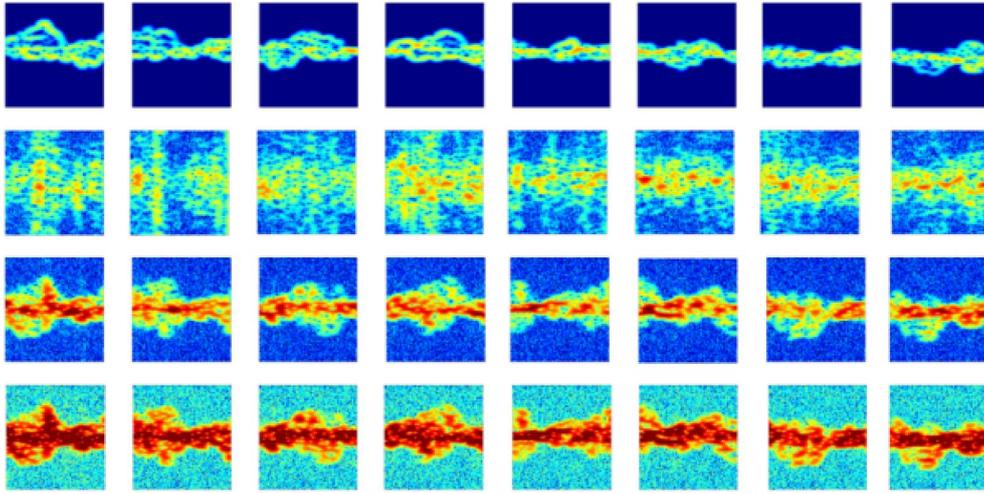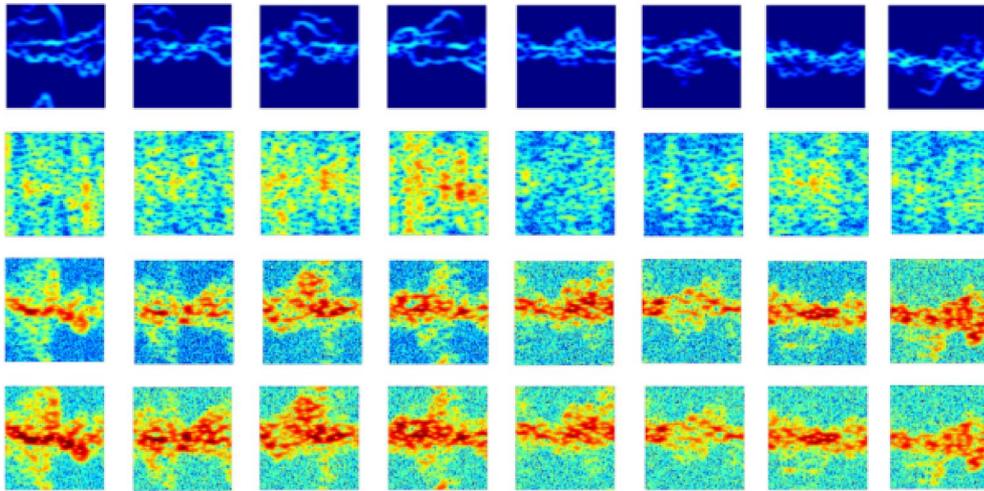
FIGURE 4 Doppler-time spectrograms of human walking in the ACR scenario with monostatic narrowband radar operating at **5 GHz**. The y-axis across all figures shows Doppler frequencies spanning from −250 to +250 Hz. The x-axis across each figure is of 0.75 s duration with a total time duration of 6 s across the eight columns. The dynamic range of each figure is from −20 to −70 dB. The first, second, third and fourth rows show the radar signature of human walking in free space, low conductive, medium conductive and high conductive wall conditions, respectively. SNR for all figures along the bottom three rows is fixed at −20 dB. ACR, around-the-corner radar; SNR, signal-to-noise ratio


FIGURE 5 Doppler-time spectrograms of human walking in ACR scenario with monostatic narrowband radar operating at **10 GHz**. Again, the signals are weaker here due to the antenna gain offset. The y-axis across all figures shows Doppler frequencies spanning from −250 to +250 Hz. The x-axis across each figure is of 0.75 s duration with a total time duration of 6 s across the eight columns. The dynamic range of each figure is from −20 to −70 dB. The first, second, third and fourth rows show the radar signature of human walking in free space, low conductive, medium conductive and high conductive wall conditions, respectively. SNR for all figures along the bottom three rows is fixed at −20 dB. ACR, around-the-corner radar; SNR, signal-to-noise ratio

to multipath, even when the target is approaching the radar (the first few columns).

Next, we present the results for the 5 GHz carrier in Figure 4. The figures show a slightly lower strength compared to the results from 2.4 GHz due to the antenna gain offset between the two frequencies. The higher carrier frequency results in finer Doppler resolution. As a result, we are able to discern distinct micro-Doppler tracks from the different body parts in the free space scenario, shown in the top row. The low conductive walls give rise to significant through-wall propagation resulting in the micro-Doppler spread and radar signal attenuation. This results in the low clarity spectrograms in the second row. Again, the third and fourth row show that the

through-wall propagation has been blocked. However, multipath reflections off the lateral walls give rise to negative Dopplers even when the target Doppler is positive with respect to radar.

In the Doppler-time spectrograms corresponding to 10 GHz, in Figure 5, we observe well resolved micro-Doppler tracks from the different body parts in the free space scenario. Due to the low sampling frequency, we also observe some aliasing at negative frequencies even for the free space scenario (first few figures along top row). The wall distortions are again considerable due to both through-wall propagation effects (for low conductive walls) and multipath off lateral walls (for the high conductive walls).
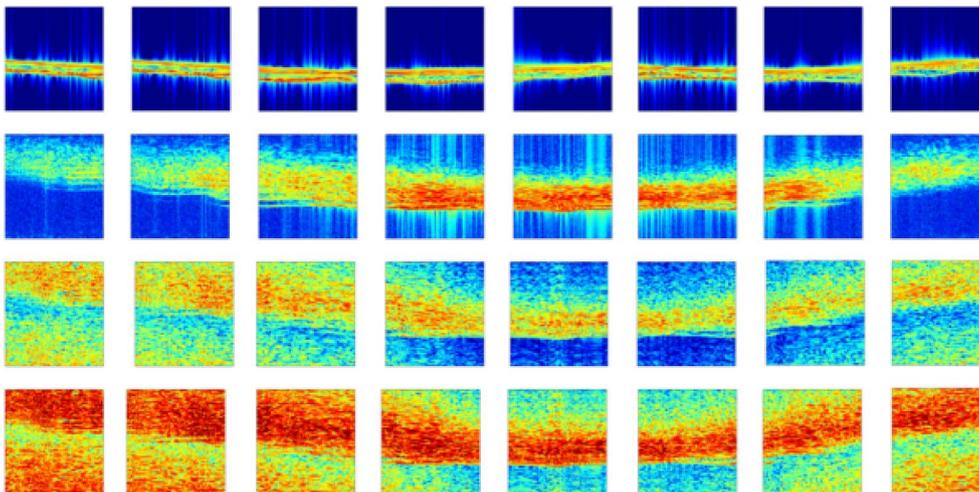
FIGURE 6 High-range resolution profile of human walking in the ACR scenario with monostatic narrowband radar operating at **2.4 GHz**. The y-axis across all figures shows a range spanning from 0 to 10 m. The x-axis across each figure is of 0.75 s duration with a total time duration of 6 s across the eight columns. The dynamic range of each figure is from −30 to −70 dB. The first, second, third and fourth rows show the radar signature of human walking in free space, low conductive, medium conductive and high conductive wall conditions, respectively. SNR for all figures along the bottom three rows is fixed at –20 dB. ACR, around-the-corner radar; SNR, signal-to-noise ratio
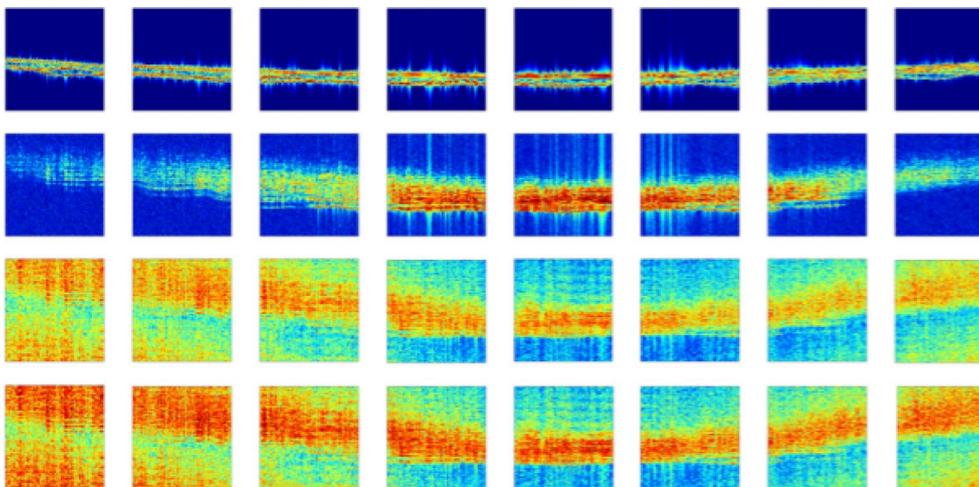
FIGURE 7 High-range resolution profile of human walking in the ACR scenario with monostatic narrowband radar operating at 5 GHz. The y-axis across all figures shows range spanning from 0 to 10 m. The x-axis across each figure is of 0.75 s duration with a total time duration of 6 s across the eight columns. The dynamic range of each figure is from −40 to −80 dB. The first, second, third and fourth rows show the radar signature of human walking in free space, low conductive, medium conductive and high conductive wall conditions, respectively. SNR for all figures along the bottom three rows is fixed at –20 dB. ACR, around-the-corner radar; SNR, signal-to-noise ratio

3.2.2 | Broadband Doppler-time Signatures

We simulated broadband radar data of 2 GHz bandwidth about the three carrier frequencies using the FDTD solver. This results in a range resolution of 0.075 m and the maximum unambiguous range, based on the frequency step size, is 10 m. Complex Gaussian noise was added to the pixels of the resulting HRRP images and a total of 1600 images were generated for each wall type. We first discuss the HRRP obtained at 2.4 GHz in Figure 6. Again, the total duration of the target motion is 6 s and is divided into eight intervals of 0.75 s each. The top row shows the target motion in free space conditions (in the absence of walls). We observe the range of the target changing only

slightly as the human is moving tangentially across the radar's field-of-view. We are able to observe fine micro-range tracks arising from the motion of the limbs. However, the images significantly deteriorate in the presence of the walls due to multipath. In the case of the low conductive wall (second row), the ringing of the signal through the wall gives rise to multipath but also attenuates the radar signal. For high, conductive walls, the multipath arises due to reflections off the lateral walls which cause the radar received signal strength to increase. We also observe considerable aliasing in these scenarios.

Similar phenomena are observed in the HRRP for 5 and 10 GHz, which are shown in Figures 7 and 8. Again, the top row in both these figures shows the HRRP when the human is
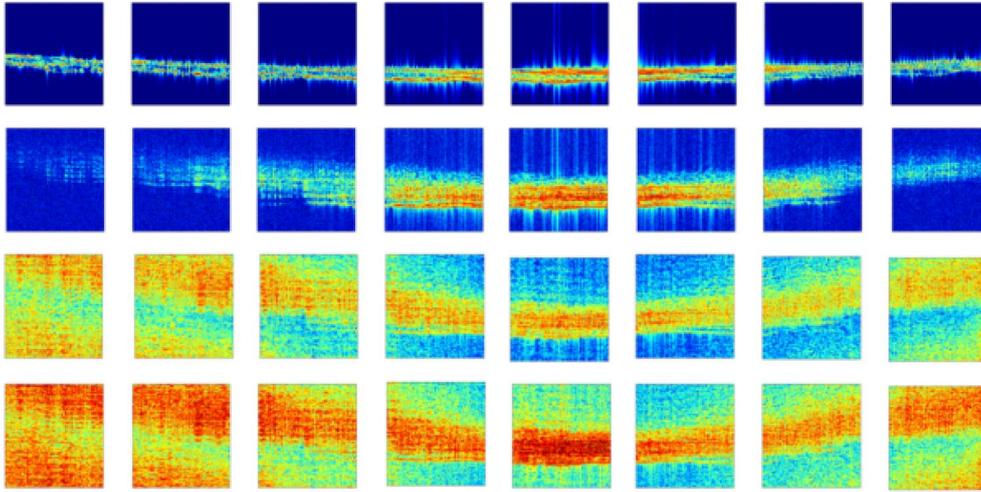
FIGURE 8   High-range resolution profile of human walking in the ACR scenario with monostatic narrowband radar operating at 10 GHz. The y-axis across all figures shows the range spanning from 0 to 10 m. The x-axis across each figure is of 0.75 s duration with a total time duration of 6 s across the eight columns. The dynamic range of each figure is from −50 to −90 dB. The first, second, third and fourth rows show the radar signature of human walking in free space, low conductive, medium conductive and high conductive wall conditions, respectively. SNR for all figures along bottom three rows is fixed at –20 dB. ACR, around-the-corner radar; SNR, signal-to-noise ratio

walking in free space conditions where there are no walls and no noise. The second, third and fourth rows show the results when the walls are of low, medium and high conductivity respectively. The HRRP show a lot of similarity across the three carrier frequencies. This is mainly because the HRRP features are a function of the range resolution and the bandwidth of the radar which are identical across the three cases. The results from 10 GHz show the greatest distortions and clutter.

4 | SIMULATION RESULTS AND ANALYSIS

In this section, we compare the similarity of the denoised/reconstructed images obtained from DAE, SparseDAE and StackedSDAE with respect to the clean ground truth images through the SSIM metric. The performances are evaluated for both types of radar signatures—the Doppler-time spectrograms and the HRRP— that were discussed above. We consider two parameters for comparison— the labelling mismatch error and the SNR, which is the ratio of the minimum signal receivable by the radar to the mean noise floor. In real-world conditions, it may be impossible to exactly replicate a target motion in free space and ACR conditions during training. Therefore, the training data may have a significant mismatch between the clean X^{tr} and the noisy and cluttered $\widehat{X}^{tr}$. We model this training error by shuffling the row entries of each column of $\widehat{X}^{tr}$ such that they no longer exactly correspond to the entries in $\widehat{X}^{tr}$. We used 70% of the total images as the training data set, and the remaining 30% as the test data set. We present the convergence of the objective function shown in equation (5) with the number of iterations in Figure 9. We then change the labelling mismatch error percentage from 0% to 60% by changing the degree of shuffling. Next, we change the SNR of the images from −15 to + 20 dB by changing the Gaussian noise power N_p that is added to each pixel of the image.
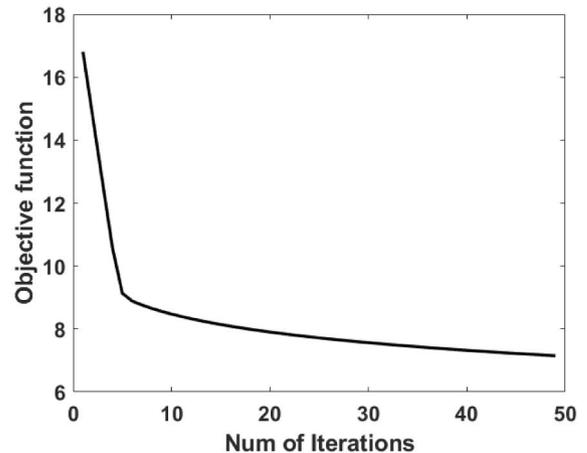

FIGURE 9   Convergence curve of the objective function for the denoising algorithm for a fixed SNR of 0 dB. SNR, signal-to-noise ratio

4.1 | Time-frequency spectrograms

Figure 10 shows the results of the three algorithms for different labelling mismatch errors across the three carrier frequencies at SNR of −10 dB. In each case, the SSIM AD for all three algorithms—DAE, SparseDAE and StackedSDAE—are significantly improved when compared to the noisy and cluttered images BD. As the label mismatch error increases, the SSIM for all three algorithms fall. However, the fall is much lower for the StackedSDAE. Even with a 50% labelling mismatch error, the SSIM of the reconstructed images is at 0.8 at 2.4 GHz (Figure 10a) and 5 GHz (Figure 10b). However, the 10 GHz scenario is a far more challenging case, where we observed a lot of multipath from lateral walls and weaker signals due to antenna gain offset. However, even here, the SSIM of the StackedSDAE is better than the SparseDAE and DAE at high labelling errors.
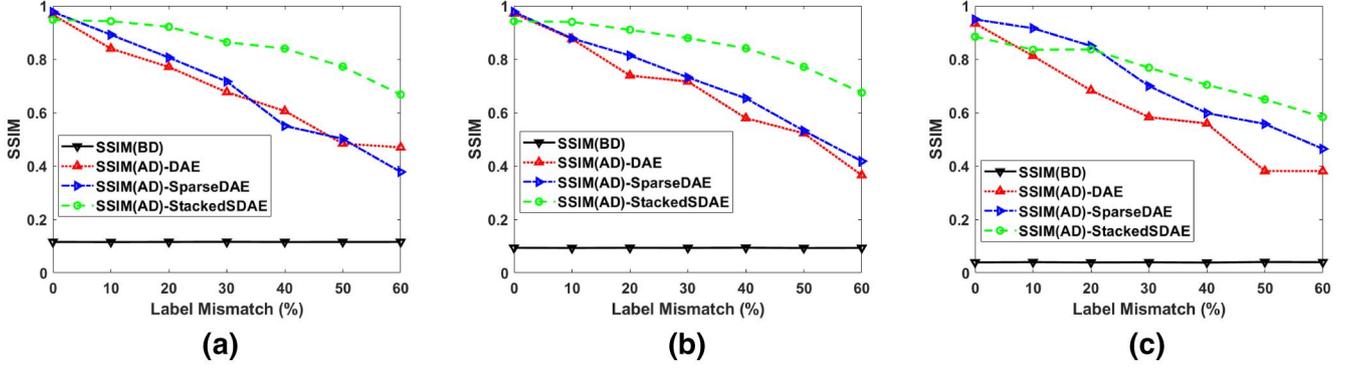
FIGURE 10 SSIM variation for spectrograms with respect to label mismatch percentage at: (a) 2.4 GHz, (b) 5 GHz and (c) 10 GHz respectively for fixed SNR of −10 dB. AD, after denoising; BD, before denoising; DAE, denoising autoencoder; SNR, signal-to-noise ratio; SSIM, structural similarity index
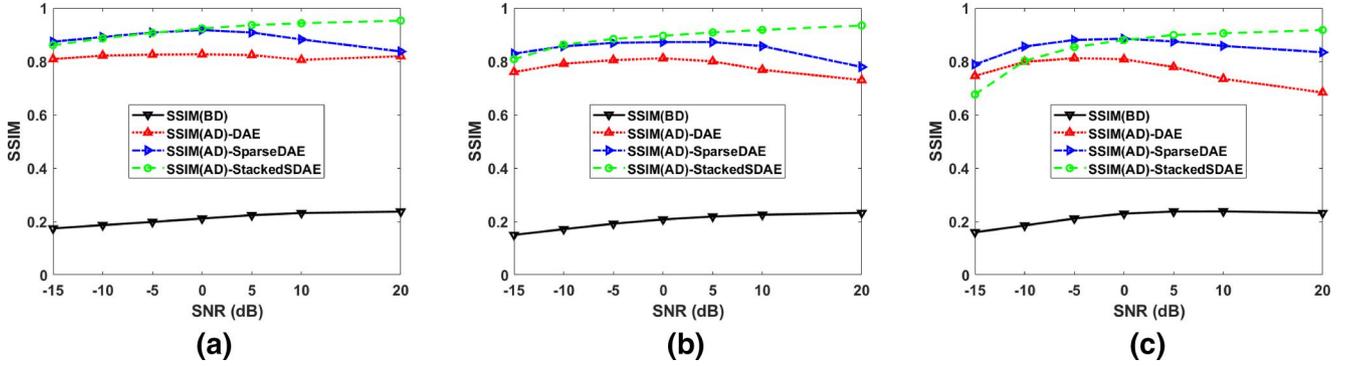

FIGURE 11 SSIM variation for spectrograms with respect to SNR at: (a) 2.4 GHz, (b) 5 GHz and (c) 10 GHz respectively for a fixed labelling error of 20%. AD, after denoising; BD, before denoising; DAE, denoising autoencoder; SNR, signal-to-noise ratio; SSIM, structural similarity index

Next, we consider the effect of SNR on the three algorithms in Figure 11. Again, there is a significant improvement in the SSIM AD for all three algorithms across all three frequencies. We observe that both the SparseDAE and the StackedSDAE are more robust to noise than DAE at low SNRs (from −15 to 5 dB) at 2.4 GHz (Figure 11a) and 5 GHz (Figure 11b). These results indicate that the use of sparsity constraints in the hidden layer representations results in increased robustness of the algorithm to Gaussian noise. Additional stacking layers also benefit for slightly higher SNR values. However, at very low SNR values (< -10 dB), in Figure 11c corresponding to 10 GHz radar frequency, additional stacking layers may be required to retain the robustness of the algorithm. The performance here is poorer due to weaker radar signals at 10 GHz due to the gain offset.

4.2 | High resolution range profiles

Next, we study the performance of the three algorithms on the HRRPs. First, we consider the label mismatch error in Figure 12 for the three carrier frequencies when SNR is −10 dB. Again, we observe that all three algorithms result in an increase in the SSIM AD compared to the SSIM of the cluttered image BD. As the labelling mismatch error increases, the SSIM falls for all three algorithms across the three

frequencies. However, the SSIM fall of the StackedSDAE is far less than DAE and SparseDAE and is at 0.75 even when the label mismatch is 50% for 2.4 GHz (Figure 12a) and 5 GHz Figure 12b. The denoising performances for all three algorithms are however significantly poorer at 10 GHz possibly because of the greater multipath and weaker signal strength. Similar trends are observed when we compare the performance of the three algorithms for varying SNR in Figure 13.

Both SparseDAE and StackedDAE are more robust than DAE at low SNR values for 2.4 GHz (Figure 13a) and 5 GHz (Figure 13b). But StackedSDAE deteriorates significantly at extremely low SNR for 10 GHz (Figure 13c) below −10 dB, due to the weaker signal strength, indicating that we may need greater depth in the hidden layers of the autoencoder.

5 | MEASUREMENT RESULTS

5.1 | Measurement data collection

In the previous sections, we demonstrated the effectiveness of the SparseDAE and StackedSDAE in denoising spectrograms and HRRPs generated in the ACR scenarios. However, these algorithms are essentially suited for denoising *any* type of radar signature. To support this claim, we evaluate these algorithms on a third type of radar signature—the range
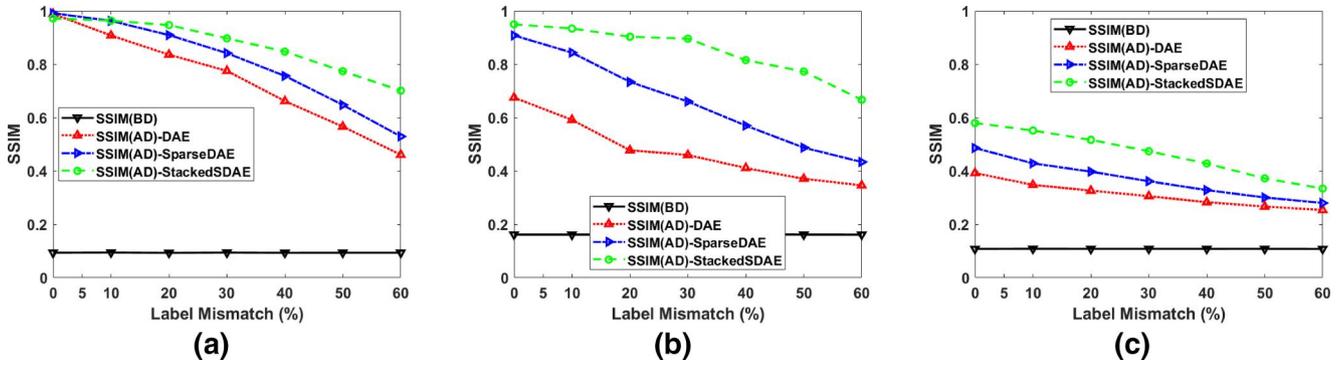
FIGURE 12 SSIM variation for HRRPs with respect to the label mismatch percentage at (a) 2.4 GHz, (b) 5 GHz and (c) 10 GHz respectively, for fixed SNR of −10 dB. AD, after denoising; BD, before denoising; DAE, denoising autoencoder; HRRP, high range resolution profiles; SNR, signal-to-noise ratio; SSIM, structural similarity index
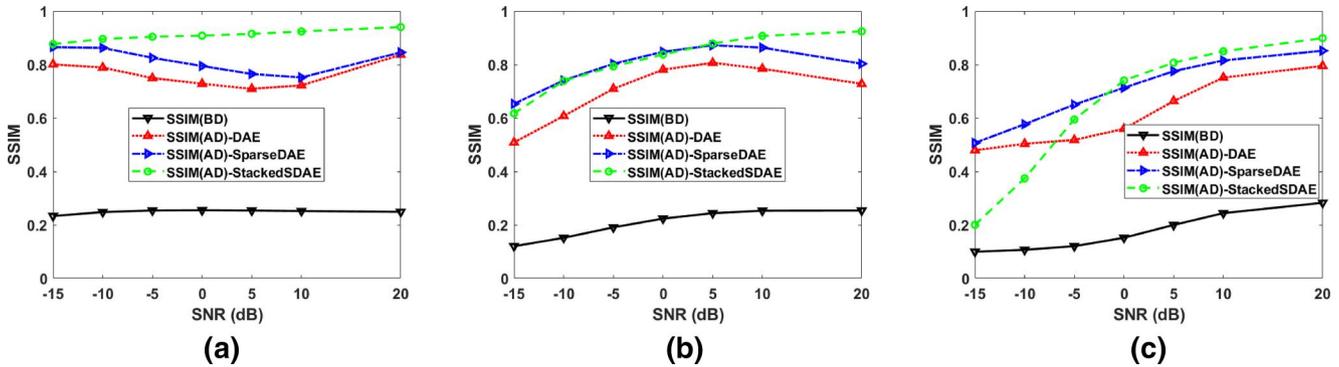

FIGURE 13 SSIM variation for HRRPs with respect to SNR at: (a) 2.4 GHz, (b) 5 GHz, and (c) 10 GHz respectively for a fixed labelling error of 20%. AD, after denoising; BD, before denoising; DAE, denoising autoencoder; HRRP, high range resolution profiles; SNR, signal-to-noise ratio; SSIM, structural similarity index

enhanced frontal images. These images are generated by processing wideband measurement data from 3.3 to 10.3 GHz captured using an imaging sensor called Walabot Pro [48]. This is an uncalibrated sensor that consists of a 4 × 4 antenna array with a maximum detectable range of about 4 m in LOS conditions and a field-of-view of approximately 90° across azimuth and elevation. The radar data cube is processed through a three-dimensional Fourier transform. Then the peaks across the range domain are superposed to obtain range-enhanced frontal images of targets. The experimental setup for our measurement data collection is shown in Figure 14. The DAE and its variants are trained with clean images of a slow-moving human subject at 2 m gathered in LOS environments and the corresponding cluttered images. The subject carries two boxes covered with aluminium tape to enhance the reflectivity from the hands.

Figure 15a shows the frontal radar image of the subject in LOS conditions where the torso, legs and arms of the human are noticeable. The experiments are performed on five subjects of different heights and girth. For each of these subjects, we captured 90 measurements at different orientations with respect to the sensor.

Due to the low transmitted power and limited dynamic range, the Walabot cannot be used in typical Indian through-wall scenarios (20 cm brick walls). Instead, we synthetically
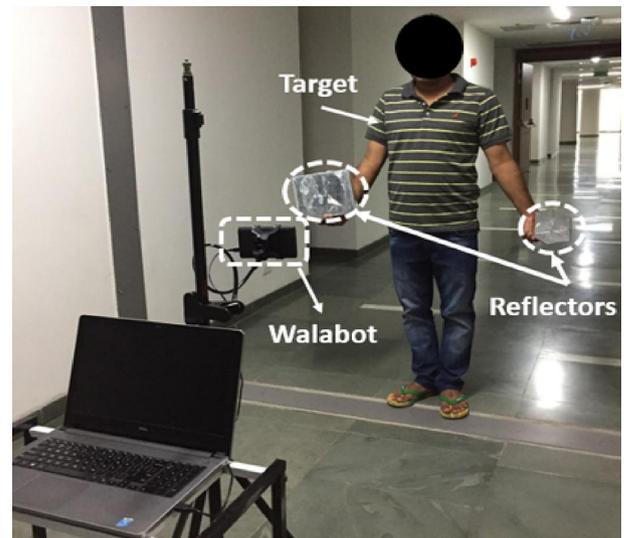

FIGURE 14 Measurement setup of frontal imaging of a slow-moving human by Walabot

corrupted the radar images with three types of distortions—additive Gaussian noise (of SNR from 0 to 30 dB), clutter, and labelling errors. We modelled the clutter as a collection of discrete point scatterers randomly distributed across the radar's
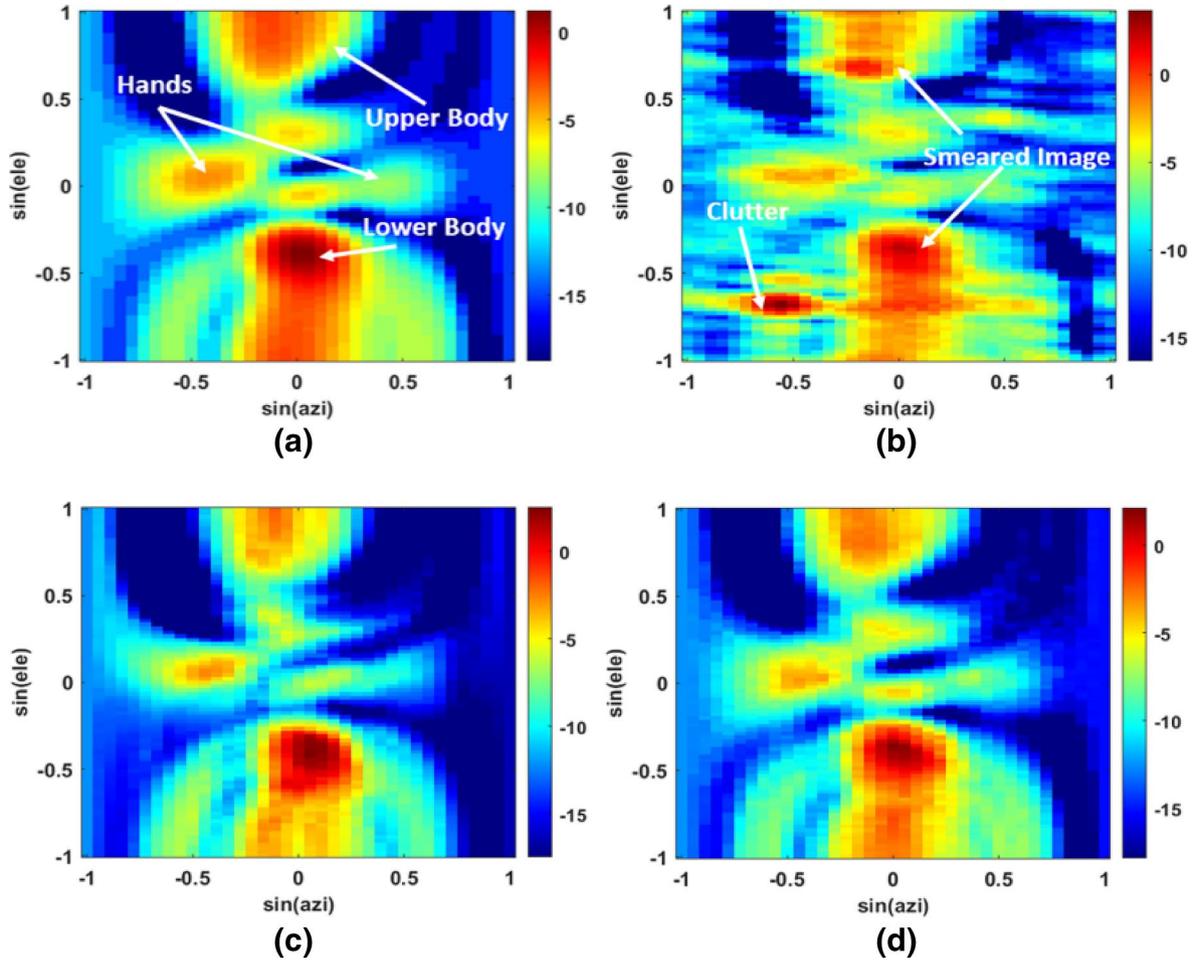
FIGURE 15 Measured range enhanced frontal images of a slow-moving human: (a) line-of-sight clean image, (b) cluttered image with SCR = 0 dB, (c),(d) reconstructed radar images after denoising for hidden layer dimensions $l_1 = 100$, and $l_2 = 500$ respectively. SCR, signal-to-clutter ratio

field-of-view whose magnitudes were varied to obtain signal to clutter ratios (SCR) spanning from 0 to 30 dB. The phase of each scatterer followed a uniform distribution across 360°. Using Binomial distribution and a probability of false alarms of 0.06, we obtain approximately five false alarms for each image. We generated the cluttered images by the complex sum of the measurement, and clutter signals. An example of the distortions introduced to the frontal image by clutter signals is shown in Figure 15b where we observe ghost targets.

We introduced labelling mismatch errors by shuffling a proportion of the labels of the clean images so that they did not correspond correctly to the corrupted images. Each of the 31 × 31 pixel images were vectorised. Then the images are stacked column-wise to obtain a [961 × 450] matrix. The data is then split into a training set (80%) and test set (20%).

5.2 | Results and analyses

The training and testing of the algorithms are carried out in Matlab 2018b on Intel(R) Core(TM) i7-5500 processor with 16-GB Ram running at 2.40 GHz. We present the results of the conventional DAE and its two variants—SparseDAE and StackedSDAE in Figure 16. In all the results, we present the SSIM between the corrupted and ground truth reference clean image BD and the SSIM between the reconstructed image and clean image AD. We observe a significant improvement in the SSIM AD for all three algorithms in all of the cases.

First, we study the effect of SNR on the denoising performance in Figure 16a. We observe that as the SNR decreases, the SSIM degrades significantly for conventional DAE. However, both SparseDAE and StackedSDAE are robust to noise since the performance does not significantly deteriorate with a fall in SNR.

The DAE is, however, less sensitive to low SCR values as observed in Figure 16b. The SparseDAE deteriorates slightly but the StackedSDAE does not get significantly impacted by low SCR values. The SSIM falls with an increase in labelling error in Figure 16c. However, the SparseDAE and StackedSDAE are less sensitive than the conventional DAE. Finally, we examine the sensitivity of the algorithms' performance to the number of nodes in the hidden layer in Figure 16d. We observe that the performance of all three algorithms converges with an increase in the number of nodes. The StackedSDAE, however, converges for the fewest number of nodes. The algorithms require a minimum number of nodes in the hidden
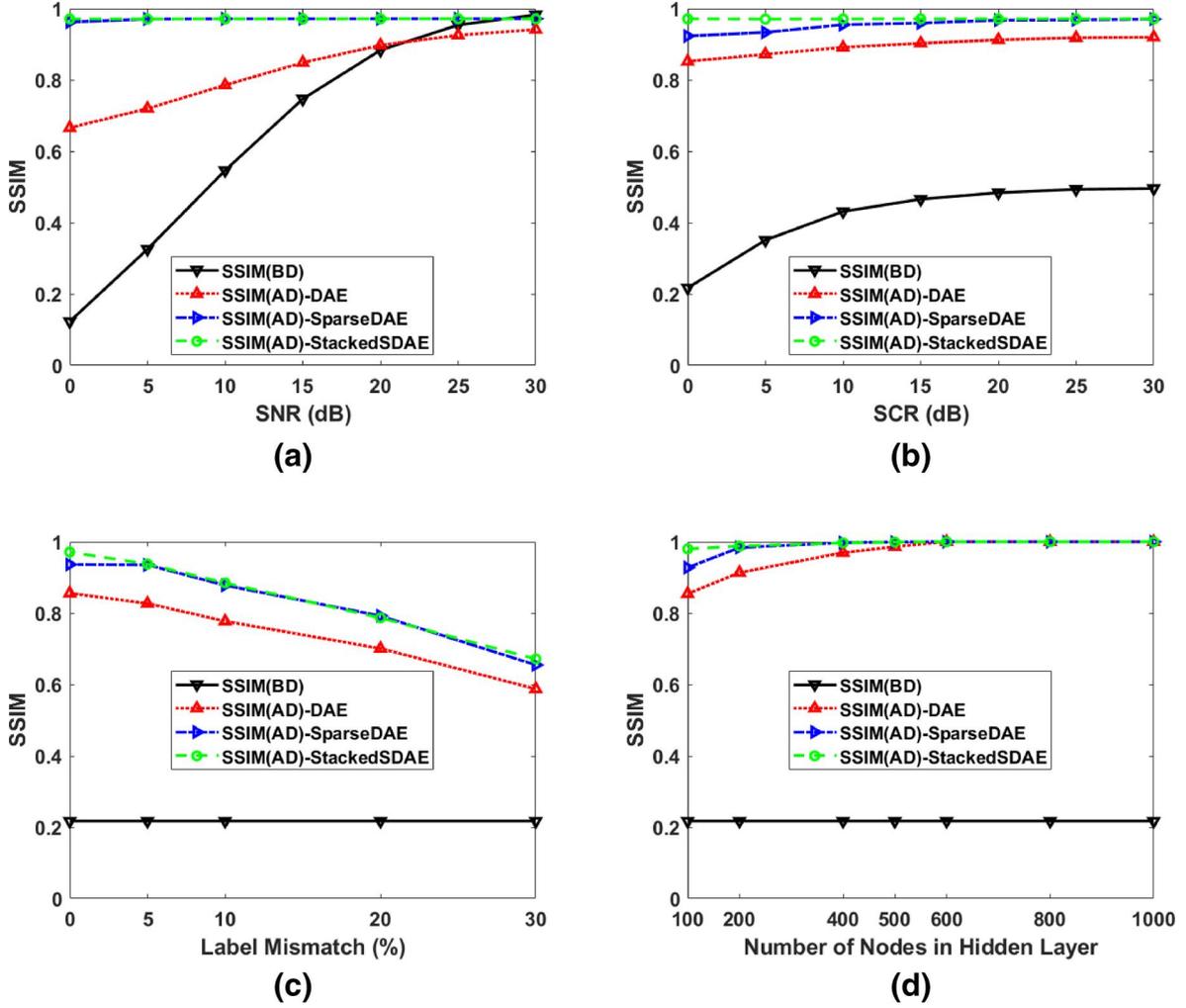
FIGURE 16 SSIM variation with respect to: (a) SNR, (b) SCR, (c) labelling mismatch error during training stage and (d) the number of nodes in the hidden layer. AD, after denoising; BD, before denoising; DAE, denoising autoencoder; SCR, signal to clutter ratio; SNR, signal-to-noise ratio; SSIM, structural similarity index

layers to achieve maximum improvement. The number of nodes is an important metric that determines the computational complexity (both time and memory) of the algorithm.

We compare the computational time complexity of the three algorithms during training and test in Table 1. While the training time of DAE and SparseDAE are comparable, the StackedSDAE takes more than twice as long to train. This is because the incorporation of stacked hidden layers results in training requirements of additional weighting matrices in the hidden layers. However, due to the feature size reduction in these matrices, there is considerably lower computation time for the StackedSDAE during the test. As a result, the StackedSDAE may be more suitable for real-time operations.

6 | BENCHMARKING WITH OTHER ALGORITHMS

We compare the performance of our algorithm, qualitatively and quantitatively, with subspace filtering based on singular value decomposition (SVD) and wavelet filtering.

TABLE 1 Computational time complexity of DAE and its variants

Algorithm	Training time (s)	Test time (ms)
DAE	205.3	76
SparseDAE	228.3	66
StackedSDAE	466.3	**0.7**

Abbreviation: DAE, denoising autoencoder.

6.1 | Subspace filtering

We have used subspace filtering methods presented in [57] to denoise the simulated time-domain data used to generate the ACR spectrograms. Using SVD, we identify the eigenvalues of the data. The top few singular vectors belong to the signal while the remaining constitute the noise subspace. Then, we reconstruct denoised spectrograms after removing the distortions arising from the lower eigenvalues. Since, the multipath clutter, in our scenario, are directly dependent on the target, they do not occupy orthogonal subspaces to the target
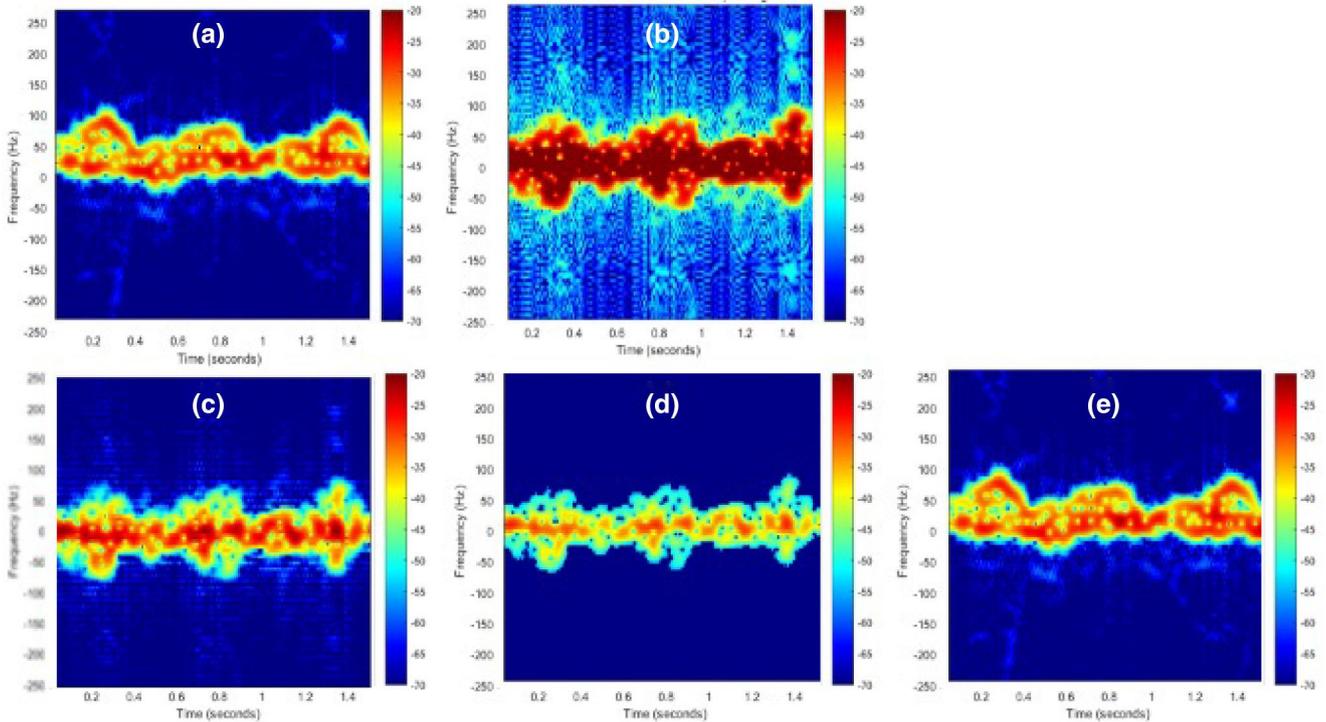
FIGURE 17 Spectrograms of humans in (a) freespace, (b) ACR scenarios. Denoised images obtained using (c) wavelet filtering, (d) subspace filtering using SVD and (e) proposed methods using sparsity-based autoencoders. ACR, around-the-corner radar; SVD, singular value decomposition

subspace. The results presented in Figure 17 clearly indicate that the SVD-based approach removes the noise but not the multipath distortions introduced in the ACR scenario, which are observed at negative Dopplers.

6.1.1 | Wavelet filtering

Next, we use wavelet-based techniques for denoising the images. We apply discrete wavelet transform on the raw time-domain data. Again, we assume that the signal returns occupy the top wavelet coefficients while the remaining coefficients correspond to the noise and distortions. Therefore, we convert these coefficients to zero and then apply inverse discrete wavelet transform to reconstruct the denoised images. The resulting images in Figure 17 again show that the algorithm is successful in removing the independent noise but not the target-dependent multipath distortions. In contrast, the proposed method based on autoencoders removes both the noise and the multipath clutter (negative Dopplers).

In Table 2, we quantitatively compare the performances of the three algorithms. We observe that BD, the average SSIM between the noisy ACR signatures and the free space signatures is 0.05 and the NMSE is 0.22. AD, the SSIM for SVD and wavelet filtering improve slightly by removing noise. However, the images still look different from the free space images due to the presence of the clutter. On the other hand, the proposed methods using autoencoders result in high SSIM (above 0.9) and a low NMSE (0.01) since they succeed in removing both noise and clutter-based distortions.

TABLE 2 Quantitative comparison of the denoising performance by subspace filtering with SVD, wavelet filtering and proposed method using autoencoders

Method	SSIM (BD)	SSIM (AD)	NMSE (BD)	NMSE (AD)
SVD	0.05	0.06	0.22	0.1
Wavelets	0.05	0.08	0.22	0.11
StackedSDAE	0.05	0.92	0.22	0.01

Abbreviations: AD, after denoising; BD, before denoising; DAE, denoising autoencoder; NMSE, normalised mean square error; SSIM, structural similarity index; SVD, singular value decomposition.

7 | CONCLUSION

Indoor radar signatures of dynamic human motions are corrupted by target-dependent and target-independent static and dynamic clutter introduced by the presence of walls and other reflecting surfaces. We have used a variant of DAE, called the StackedSDAE, that incorporates both sparsity and depth in the hidden layer representations of the noisy images for clutter mitigation. The encoder and decoder stages of the algorithm are trained with labelled clean and noisy data. No additional information of the wall geometry or characteristics are required for the algorithm. Due to the additional stacked layers within the hidden layers, the training time for this algorithm is greater than that of the conventional DAE. However, each additional stacked layer has fewer nodes than the previous layer. This results in lowered feature size of the final representation and lower test time operation. The resulting denoised images are

structurally similar to the radar images of the target that would have been obtained in free space scenarios. The StackedSDAE is more robust than the conventional DAE to labelling mismatch error between clean and noisy images during training. The algorithm is also more robust to low SNR (-10 to $+5$ dB) than the conventional DAE. For example, in the case of the simulated ACR signatures, the denoised images have an SSIM above 0.75 even when the SNR is -10 dB and the label mismatch error is 50%. At extremely low SNR (below -0 dB), we observe some deterioration in the performance possibly indicating that greater number of hidden layers are required at these SNRs. The complete database of radar signatures and algorithms are shared with the research community on the following URL https://rb.gy/mmhzf6.

ORCID
Shobha Sundar Ram ID https://orcid.org/0000-0002-0265-8610

REFERENCES

1. Amin, M.G.: Through-the-wall Radar Imaging. CRC Press Boca Raton (2016)
2. Amin, M.: Radar for Indoor Monitoring: Detection, Classification, and Assessment. CRC Press Boca Raton (2017)
3. Gurbuz, S.Z., Amin, M.G.: Radar-based human-motion recognition with deep learning: promising applications for indoor monitoring. IEEE Signal. Process. Mag. 36(4), 16–28 (2019)
4. Le Kernec, J., et al.: Radar signal processing for sensing in assisted living: the challenges associated with real-time implementation of emerging algorithms. IEEE Signal Process. Mag. 36(4), 29–41 (2019)
5. Thayaparan, T., Stanković, L., Djurović, I.: Micro-Doppler-based target detection and feature extraction in indoor and outdoor environments. J. Franklin Inst. 345(6), 700–722 (2008)
6. Fioranelli, F., Ritchie, M., Griffiths, H.: Classification of unarmed/armed personnel using the netrad multistatic radar for micro-Doppler and singular value decomposition features. IEEE Geosci. Remote Sens. Lett. 12(9), 1933–1937 (2015)
7. Chen, V.C., et al.: Analysis of micro-Doppler signatures. IEE Proc. Radar, Sonar Navig. 150(4), 271–276 (2003)
8. Ram, S.S., et al.: Doppler-based detection and tracking of humans in indoor environments. J. Franklin Inst. 345(6), 679–699 (2008)
9. Narayanan, R.M., et al.: Through-the-wall detection of stationary human targets using Doppler radar. Prog. Electromagn. Res. B. 20, 147–166 (2010)
10. Clemente, C., et al.: Developments in target micro-Doppler signatures analysis: radar imaging, ultrasound and through-the-wall radar. EURASIP J. Adv. Signal Process. 2013(1), 47 (2013)
11. Ram, S.S., Hao Ling, H.: Through-wall tracking of human movers using joint Doppler and array processing. IEEE Geosci. Remote Sensing Lett. 5(3), 537–541 (2008)
12. Lin, A., Ling, H.: Frontal imaging of human using three- element Doppler and direction-of-arrival radar. Electron. Lett. 42(11), 660–661 (2006)
13. Ram, S.S., Majumdar, A.: High-resolution radar imaging of moving humans using Doppler processing and compressed sensing. IEEE Trans. Aero. Electron. Syst. 51(2), 1279–1287 (2015)
14. Ahmad, F., Amin, M.G., Kassam, S.A.: Synthetic aperture beamformer for imaging through a dielectric wall. IEEE Trans. Aero. Electron. Syst. 41(1), 271–283 (2005)
15. Dehmollaian, M., Sarabandi, K.: Refocusing through building walls using synthetic aperture radar. IEEE Trans. Geosci. Remote Sens. 46(6), 1589–1599 (2008)
16. Ahmad, F., Yimin Zhang, Y., Amin, M.G.: Three-dimensional wideband beamforming for imaging through a single wall. IEEE Geosci. Remote Sens. Lett. 5(2), 176–179 (2008)
17. Yoon, Y.-S., Amin, M.G.: High-resolution through-the-wall radar imaging using beamspace music. IEEE Trans. Antenn. Propag. 56(6), 1763–1774 (2008)
18. Cammenga, Z.A., et al.: High range resolution micro-Doppler analysis. In: Proceedings of SPIE Defense+ Security. (International Society for Optics and Photonics), 94611G (2015)
19. Martone, A., et al.: Through-the-wall detection of slow-moving personnel. In: Proceedings of SPIE Defense+ Security, 73080Q. International Society for Optics and Photonics (2009)
20. Ahmad, F., Amin, M.G.: Through-the-wall human motion indication using sparsity-driven change detection. IEEE Trans. Geosci. Remote Sens. 51(2), 881–890 (2013)
21. Gennarelli, G., et al.: Multiple extended target tracking for through-wall radars. IEEE Trans. Geosci. Remote Sens. 53(12), 6482–6494 (2015)
22. He, Y., et al.: Range-Doppler surface: a tool to analyse human target in ultra-wideband radar. IET Radar, Sonar Navig. 9(9), 1240–1250 (2015)
23. Fogle, O.R., Rigling, B.D.: Micro-range/micro-Doppler decomposition of human radar signatures. IEEE Trans. Aero. Electron. Syst. 48(4), 3058–3072 (2012)
24. Erol, B., Amin, M.G.: Radar data cube processing for human activity recognition using multisubspace learning. IEEE Trans. Aerosp. Electron. Syst. 55(6), 3617–3628 (2019)
25. Zhao, M., et al.: Through-wall human pose estimation using radio signals. In: Proceedings of the IEEE Conference on Computer Vision and Pattern Recognition, pp. 7356–7365.Salt Lake City, UT, (2018)
26. Sume, A., et al.: Radar detection of moving objects around corners. In: Proceedings of SPIE Defense + Security, 73080V. International Society for Optics and Photonics, Orlando, FL (2009)
27. Sume, A., et al.: Radar detection of moving targets behind corners. IEEE Trans. Geosci. Remote Sens. 49(6), 2259–2267 (2011)
28. Rabaste, O., et al.: Around-the-corner radar: detection of a human being in non-line of sight. IET Radar, Sonar Navig. 9(6), 660–668 (2015)
29. Thai, K.P.H., et al.: Around-the-corner radar: detection and localization of a target in non-line of sight. In: Proceedings of the IEEE Radar Conference (RadarConf), pp. 0842–0847. IEEE, Seattle, WA (2017)
30. Vishwakarma, S., et al.: Micro-Doppler signatures of dynamic humans from around the corner radar. In: Proceedings of the IEEE International Radar Conference (RADAR), pp. 169–174. IEEE,Washington, DC (2017)
31. Ahmad, F., Amin, M.G., Mandapati, G.: Autofocusing of through-the-wall radar imagery under unknown wall characteristics. IEEE Trans. Image Process. 16(7), 1785–1795 (2007)
32. Leigsnering, M., et al.: Multipath exploitation in through-the-wall radar imaging using sparse reconstruction. IEEE Trans. Aero. Electron. Syst. 50(2), 920–939 (2014)
33. Vishwakarma, S., et al.: Mitigation of through-wall interference in radar images using denoising autoencoders. In: Proceedings of the IEEE International Radar Conference, pp. 1543–1548. IEEE (2018)
34. Vishwakarma, S., Ram, S.S.: Mitigation of through-wall distortions of frontal radar images using denoising autoencoders. IEEE Trans. Geosci. Rem. Sens. 58(9), 6650–6663 (2020)
35. Chen, X., Chen, W.: Multipath ghost elimination for through-wall radar imaging. IET Radar Sonar Navig. 10(2), 299–310 (2016)
36. Tan, Q., et al.: Multipath ghost suppression for through-the-wall radar. IEEE Trans. Aero. Electron. Syst. 50(3), 2284–2292 (2014)
37. Leigsnering, M.: Sparsity-based Multipath Exploitation for Through-the-wall Radar Imaging. Springer Cham, (2018)
38. Tang, V.H., Bouzerdoum, A., Phung, S.L.: Multipolarization through-wall radar imaging using low-rank and jointly-sparse representations. IEEE Trans. Image Process. 27(4), 1763–1776 (2017)
39. Vishwakarma, S., Ram, S.S.: Detection of multiple movers based on single channel source separation of their micro-Dopplers. IEEE Trans. Aero. Electron. Syst. 54(1), 159–169 (2017)

40. Vincent, P., et al.: Stacked denoising autoencoders: learning useful representations in a deep network with a local denoising criterion. J Mach. Learn. Res. 11, 3371–3408 (2010). http://dl.acm.org/citation.cfm?id=1756006. 1953039

41. Vincent, P., et al. Extracting and composing robust features with denoising autoencoders. In: Proceedings of the 25th International Conference on Machine Learning, pp. 1096–1103. ACM, Helsinki, Finland (2008)

42. Hinton, G.E., Salakhutdinov, R.R.: Reducing the dimensionality of data with neural networks. Science. 313(5786), 504–507 (2006)

43. Sakurada, M., Yairi, T: Anomaly detection using autoencoders with nonlinear dimensionality reduction. In: Proceedings of the MLSDA 2014 2nd Workshop on Machine Learning for Sensory Data Analysis, Gold Coast Australia, pp. 4. ACM, (2014)

44. Socher, R., et al.: Dynamic pooling and unfolding recursive autoencoders for paraphrase detection. In: Proceedings of the 24th International Conference on Neural Information Processing Systems, pp. 801–809. Granada, (2011)

45. Chen, M., et al.: Marginalized denoising autoencoders for domain adaptation. In: Proceedings of the 29th International Conference on Machine Learning, pp. 1627–1634. Edinburgh, (2012)

46. Ng, A., et al.: Sparse autoencoder. CS294A Lecture Notes. 72(2011), 1–19 (2011)

47. Vishwakarma, S., Pandey, N., Ram, S.S.: Clutter mitigation in range enhanced radar images using sparsity based denoising autoencoders. In: Proceedings of the International Radar Conference (RADAR), pp. 1–6. IEEE, Toulon, (2019)

48. Walabot.. https://cdn.sparkfun.com/assets/learn_tutorials/7/2/4/ walabot-tech-brief-416.pdf/ (2017). Accessed 18 Jan 2020

49. Mehta, J., et al.: Stacked robust autoencoder for classification. In: Proceedings of the International Conference on Neural Information Processing, Springer, pp. 600–607. Kyoto, (2016)

50. Majumdar, A.: Graph structured autoencoder. Neural Netw. 106, 271–280 (2018)

51. Boyd, S., et al.: Distributed optimization and statistical learning via the alternating direction method of multipliers. Found. Trends Mach. Learn. 3(1), 1–122 (2011)

52. Bishop, C.M.: Pattern recognition. Mach. Learn. 128, 1–58 (2006)

53. Wang, Z., et al.: Image quality assessment: from error visibility to structural similarity. IEEE Trans. Image Process. 13(4), 600–612 (2004)

54. Smith, S.M., Furse, C.: Stochastic FDTD for analysis of statistical variation in electromagnetic fields. IEEE Trans. Antenn. Propag. 60(7), 3343–3350 (2012)

55. Ram, S.S., Ling, H.: Simulation of human microdopplers using computer animation data. In: Proceedings of the IEEE Radar Conference. ,pp. 1–6. IEEE, Rome, (2008)

56. Ram, S.S., et al.: Simulation and analysis of human micro-Dopplers in through-wall environments. IEEE Trans. Geosci. Remote Sens. 48(4), 2015–2023 (2010)

57. Tivive, F.H.C., et al.: Wall clutter mitigation based on eigen-analysis in through-the-wall radar imaging. In: Proceedings of the 17th International Conference on Digital Signal Processing, pp. 1–8.IEEE, Corfu, (2011)